IEEE Access
Multidisciplinary | Rapid Review | Open Access Journal

Received July 5, 2019, accepted August 14, 2019, date of publication September 20, 2019, date of current version October 3, 2019.

Digital Object Identifier 10.1109/ACCESS.2019.2942525

Three-Dimensional Numerical Study of Particle Trajectory in Particle Charge and Size Analyzer Considering the Effects of System Parameters

LU ZHANG[1], (Member, IEEE), AND JANUSZ KULON[2], (Senior Member, IEEE)
[1]College of Information Engineering, Shanghai Maritime University, Shanghai 201306, China
[2]Faculty of Computing, Engineering and Science, University of South Wales, Pontypridd CF37 1DL, U.K.

Corresponding author: Lu Zhang (luzhang@shmtu.edu.cn)

This work was supported in part by the National Natural Science Foundation of China under Grant U1701265 and Grant 61463016, and in part by the National Key Research and Development Plan under Grant 2018YFC1200200 and Grant 2018YFC1200205.

ABSTRACT In this study, for the purpose of the optimization of the measurement system performance, a three-dimensional numerical model of the particle charge and size analyzer (PCSA) is presented. The PCSA is capable of simultaneous particle size and charge measurement using phase Doppler anemometry. Numerical simulations of particle transport under the influence of the square-wave excitation field have been carried out to identify the optimal PCSA system configurations, improve the particle detection rate, and minimize the measurement bias due to experimental conditions. For the first time, the three-dimensional (3-D) numerical model was used to study the effects of excitation frequency, magnitude of the electric field, and particle inlet velocity on the particle detection rate and charge and size measurement bias. The airflow and the particle motion in the measurement cell were investigated using commercial FLUENT 14.5 software and the particle detection and validation algorithm was implemented in MATLAB. The particle phase was modelled using the Lagrangian approach. The effect of the electric field on particle trajectories was analyzed by solving a coupled system of the electric field and particle transport equations using the User-Defined-Functions (UDFs) in FLUENT. The model was validated by comparing the numerical results with reported experimental data. This 3-D numerical simulation provides a valuable insight into various tradeoffs between the detection rate of particles with different electrical mobility levels and the PCSA parameters. The numerical simulation results demonstrate that the reduction of the measurement bias of particle charge and size distribution can be achieved while maintaining high particle detection percentage by an appropriate selection of system parameters, leading to a more representative profile of measured aerosols. It is shown that the optimal ranges of the excitation frequency, magnitude of electric field, and particle velocity at inlet are between 40 – 50 Hz, 0.3 – 0.4 MV/m, and 0.01 – 0.03 m/s, respectively.

INDEX TERMS Medical aerosol, particle charge and size measurement, phase Doppler anemometry (PDA), numerical simulation.

I. INTRODUCTION

In many industrial applications, the size and electrostatic charge distribution of aerosol particles are of great significance. It has been demonstrated that the electrostatic charge, both magnitude and polarity, and size distribution of particles highly influence the particles' dispersion characteristics and can considerably alter the respiratory deposition of medical aerosol in human airways [1]. The design of drug administration devices by inhalation and medications in the future can benefit from the measurement of pharmaceutical particles in terms of their electrostatic properties and size distribution [2]. Owing to the rapidly evolving and dynamic nature of aerosols released from highly pressurized medical inhalers, it is important to simultaneously measure the size and also charge distribution of these aerosols in real time [2]. However, in comparison with the particle size measurement, the reliable simultaneous size and charge measurement still remains a significant challenge. The most widely available commercial method for simultaneous net charge

The associate editor coordinating the review of this manuscript and approving it for publication was Gang Mei.

measurements and mass quantifications is electrical low pressure impactor (ELPI) [3]. The principles governing the operation of the ELPI were used in the recent development of the modified electrical Next Generation Impactor (eNGI) to quantify simultaneously the bipolar charge and mass of aerosol particles collected from commercial medical inhalers [3]. Although eNGI is effective in detecting the instances of bipolarities of populations of particles, it lacks the capacity for simultaneous charge and size characterization of individual particles. The electrical single particle aerodynamic relaxation time (E-SPART) analyzer designed using the laser Doppler velocimetry (LDV) [4] is the only commercially available device which is capable of real-time, non-intrusive measurement of the aerodynamic size and electrostatic charge on an individual particle basis. Although the E-SPART analyzer exhibits very good measurement accuracy, it suffers from several drawbacks, such as low particle count rate because of the strict particle residency criteria inside the measurement volume [4]–[6]. This drawback could lead to measurement bias, especially in the case of non-uniform, rapidly evolving particle flows.

The particle charge and size analyzer (PCSA) developed and tested in laboratory by the authors of this paper [7] is also able to non-intrusively and simultaneously measure particle size and charge in real time. The PCSA utilizes the phase Doppler anemometry (PDA) to simultaneously measure particle charge (both magnitude and polarity) and particle size by analyzing its response to an external electric field. Since the PCSA is based on the PDA, which allows for optical rather than aerodynamic measurement of particle size, this analyzer is capable of operating with a higher data rate of analyzed particles [8]. An experimental study conducted by Kulon *et al*. [8] successfully used the PCSA to simultaneously measure the size and charge distribution of aerosol droplets from a Medic-Aid Sidestream nebulizer in a dc electric field. The work was further extended by Beleca *et al*. [9] to the measurement of the charge and size distribution of non-spherical pharmaceutical powders. Furthermore, the PCSA operated in an oscillatory electric field has been implemented [7], which offers better performance than the version using dc field excitation [10].

The performance of the PCSA depends on many parameters including particle flow properties, electric field characteristics, the size and geometry of the measurement cell, and the specific optical setup of the PDA. For many years, there have been a number of studies concerning the possible origins of uncertainty and bias in particle velocity and size measurement using the LDV/PDA, such as the measurement volume effect, slit effect, particle flow characteristics, data acquisition parameters (e.g., number of samples) for convergence statistics, and signal processing. The impacts of particle statistics on the capacity of a phase Doppler instrument to accurately measure the complex aerosol flows were studied by Edwards *et al*. [11]. Fuchs *et al*. investigated the statistical bias in estimations of flow velocity because of the spatially and temporally non-homogeneous aerosol flows [12]. Statistical errors in analyzing raw LDV signals were studied for both homogeneous and non-homogeneous seeding conditions in [13]. Davis *et al*. demonstrated that the results of size and velocity estimation were strongly biased with non-optimal configuration in the PDA system [14]. Consequently, during the design of a novel measurement system, it is necessary to optimize the system parameters in order to improve the measurement accuracy. In previous research, the influences of the optical parameters of the PDA system including fringe spacing [15]–[19], PDA geometric configurations [20], size of the measurement volume [21], and particle number concentration [16] on the accuracy of particle size measurement had been discussed and evaluated. The unsuitable aperture mask and optical lens configuration could considerably bias the diameter measurements and also slightly impact the velocity measurements in the PDA [19]. R. Payri *et al*. explored the influence of PDA system setup combination on the accuracy of particle properties measurement and the proportion of the detected and measured particles [22]. Parametric studies were performed in terms of the optical parameters, slit aperture, SNR threshold, etc. The optimal system configuration was suggested based on a set of experimental tests in different conditions [22]. It was shown that the measurement uncertainty of the LDV depended on the number of fringes inside the measurement volume, seeding concentration, measurement time, flow velocity, scattered light power, efficiency of the photo detector, etc., and these factors should be considered in system optimization [23].

Despite various advances that have been made in the aerosol velocity and size measurement using the PDA/LDV, there have been no 3-D numerical investigations on the effects of the external oscillatory electric field and the particle inlet velocity on the particle size and charge measurement using PDA. Such effects could be evaluated in terms of number of detected particles and the bias in measured particle charge and size distribution. The main research hypothesis of our paper is that better statistical representation of the attributes of particle group can be obtained by optimizing the system parameters. Because it is impractical to experimentally evaluate the influences of many system configurations on the measurement performance due to a vast amount of experimental work required, the numerical analysis of particle trajectories in the presence of an external electric field for different system parameters was used to address this problem more effectively.

Many numerically studies on the motion of charged particles in an electric field have been reported for various industrial applications including electrostatic precipitators (ESPs) [24], electrostatic separators [25], [26], electrostatic enhanced air filters [27], and electrostatic painting systems [28]. In the ESPs, the electrical force is regarded as the dominant factor influencing the particle motion. The collection efficiency of ESP has been numerically investigated by considering different parameters in many studies. N. Farnoosh *et al*. developed a 3-D numerical model of ESP to study all essential phenomena including the electric field, space charge, flow pattern, particle motion [29], [30].

The effects of inlet velocity, particle diameter, and particle concentration on the ESP collection were investigated. It was demonstrated that the particle collection efficiencies increased for the larger particles and were not strongly affected by the EHD flow [29]. The simulation results indicated that the increase in particle concentration led to more turbulent airflow and higher collection efficiency of small particles [30]. A numerical model of ESP was developed by Q. Lu *et al*. to investigate the charging and trajectories of fine particles considering both drag and Coulomb force in ESP [31]. The lower gas velocity led to higher collecting efficiencies for all sizes of particles ranging from 0.1 to 5 μm. It was shown that the acquired charges and the collection of particles larger than 1 μm were improved by increasing voltage applied at the electrodes. Numerical simulation of charging and transport of submicron particles in the ESP with multiple wire electrodes was recently reported by M. Dong *et al*. considering the applied voltage, inlet height, wire spacing, and precipitator structure [32]. It was found that the particle trapping can be improved by increasing voltage, particle size, and selecting wire spacing less than 150 mm. Furthermore, the particle trapping efficiency was also strongly affected by injection position and electrode arrangement.

The previous simulation results published in [10] by the authors of this paper showed the advantages of the oscillatory field over dc excitation in terms of the ability to capture more highly charged particles, improvement in the aerosol sampling efficiency and simplification of the measurement volume traversing mechanism. Preliminary numerical analysis using MATLAB indicated that the number of particles detected inside the measurement volume should be greater for square-wave than for sine-wave field, leading to a more representative profile of the particle electrostatic charge and size distribution [33]. However, the numerical results relied on many simplified assumptions such as two-dimensional (2-D) geometry of the measurement cell, idealized laminar flow profile, and a simplified model of particle trajectories due to the assumption of constant particle and flow velocities in the vertical direction, all of which rendered such results as only approximate and tentative [33]. A more realistic model of particle transport inside the measurement cell is required.

This paper presents a detailed analysis of transport, detection, and validation of charged particles with different mobility levels inside the measurement volume with an external excitation field taking into consideration various system parameters. A 3-D numerical modelling has been carried out using FLUENT and MATLAB commercial packages with the aim of optimizing the system performance in terms of the measurement accuracy, particle detection efficiency, and measurement bias. The paper is organized as follows. First, the 3-D computational model of the measurement cell and particle excitation system in the square-wave excitation field is described. Second, the 3-D numerical simulation results of particle trajectories inside the measurement cell are presented. Third, the effects of different system parameters on the number of particles detected inside the measurement volume and the measurement bias of particle charge and size distribution are discussed. Finally, the optimal ranges of system configurations of the PCSA for the square-wave excitation method are determined with respect to the number of detected particles and the measurement bias.

II. THEORY

A. MODEL DESCRIPTION

The simplified diagram of the PCSA measurement system illustrating the measurement principle is shown in Fig. 1.

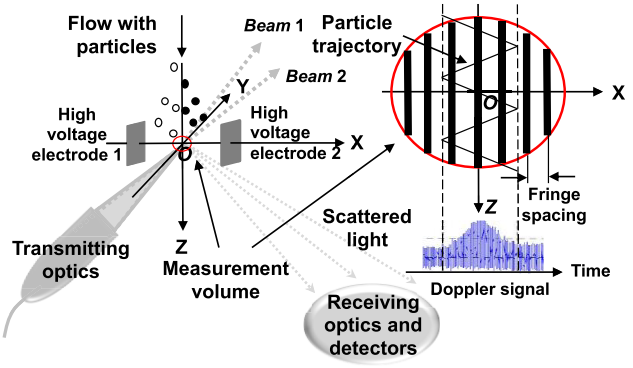

FIGURE 1. Diagram of optical setup of the PCSA system.

In the measurement cell of the PCSA system, the intersection of two laser beams creates the measurement volume in the intersection region. Owing to the intensity decay of the interference structure, the measurement volume [15] is arbitrarily defined by the following equation:

$$\left[\frac{x_{op}\cos\left(\frac{\theta}{2}\right)}{r_w}\right]^2+\left[\frac{y_{op}\sin\left(\frac{\theta}{2}\right)}{r_w}\right]^2+\left[\frac{z_{op}}{r_w}\right]^2=1 \quad (1)$$

where x_{op}, y_{op}, and z_{op} are the coordinates of the particle positions in X, Y, and Z directions, respectively, r_w is the Gaussian beam radius at waist, and θ is the intersection angle of laser beams.

During the 3-D numerical modelling, the particles entered into the measurement cell from a cylindrical inlet. The charged particle motion within the measurement cell was assumed to be mainly influenced by the electrical force caused by the external electric field, the drag force due to the air viscosity and the gravitational force. Owing to the low volume fraction of particles (i.e. the dispersed phase of the system is sufficiently dilute) assumed in the measurement cell of the PCSA, the particle–particle interaction and the impact of the particle volume fraction on the gas phase was neglected in this 3-D approach. The charged particles were subjected to the square-wave excitation field created between two parallel-plate electrodes. Some of these particles were successfully detected inside the measurement volume and scattered light, which was received by three photo detectors at different positions in the PDA system. As a result, three Doppler burst signals (DBSs) with different phases and the same frequency were generated. The information of

instantaneous particle velocity, size and bipolar charge can be extracted from the instantaneous Doppler frequency and the phase shift between the DBSs. The number of particles detected inside the volume can be significantly affected by the particle diameter and charge, drive frequency, field magnitude, and particle velocity at inlet. The influences of these factors on the particle detection percentage and measurement bias are discussed in the following sections of this paper. A 3-D geometrical model created in FLUENT for the numerical simulation of particle motion inside the measurement cell is shown in Fig. 2.

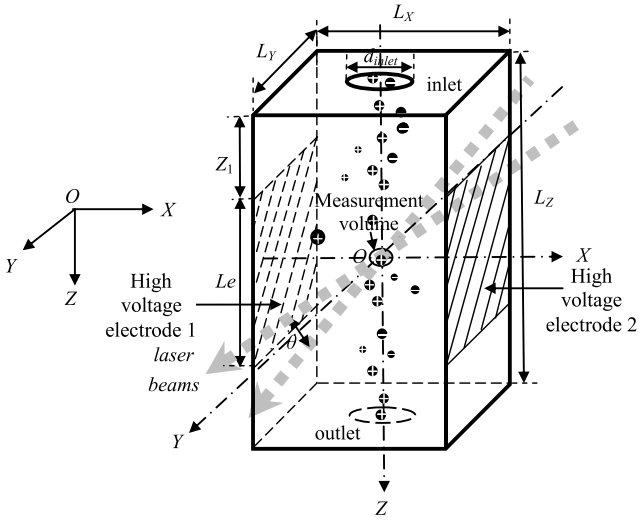

FIGURE 2. Three-dimensional computational model of the measurement cell.

As can be seen in Fig. 2, the 3-D model is established in Cartesian coordinates with $-10 < x < 10$ (mm), $-10 < y < 10$ (mm) and $-20 < z < 20$ (mm). The distance between the two electrodes is 20 mm. The sizes of the electrodes in Y and Z directions are L_Y and L_e, respectively, and $L_Y = L_e = 20$ mm. The distance between the inlet and the electrode is $Z_1 = 10$ mm. d_{inlet} denotes the diameter of the inlet. The centre of the measurement cell is exactly the same as the centre of the measurement volume and is also at the origin of the Cartesian coordinate system. In the X–Y plane, the incident laser beams intersect at the origin with the angle θ. In the measurement cell, the bipolarly charged particles move in the X–Z plane and travel back and forth under the effect of the electrical force due to the oscillatory field.

B. ELECTRIC EXCITATION FIELD

The square-wave excitation method was considered in the 3-D numerical simulation. With the assumption of the external excitation field applied in X direction in the model, the instantaneous electrical force, $F_{X\_square}(t)$ in the square-wave excitation field, can be given as follows:

$$F_{X\_square}(t) = \begin{cases} E_X q & 0 \le t < \dfrac{T}{2} \\ -E_X q & \dfrac{T}{2} < t \le T \end{cases} \tag{2}$$

where E_X is the strength of the electric field in X direction, q denotes the charge on an individual particle, and T is the period of the square-wave excitation. The electrical forces acting on the particles were added to each single volume cell of the discretized FLUENT model using User-Defined-Functions (UDFs).

C. AIRFLOW MODEL

Because of the limited variation in pressure and temperature in the measurement cell of the PCSA, the ambient air in the cell was modelled as an incompressible Newtonian fluid. In the measurement cell, the density and viscosity of the air were maintained constant and the flow was laminar. The fluid phase fulfills the continuity equation and the Navier–Stokes equations were solved using FLUENT 14.5 software.

D. PARTICLE TRAJECTORY

The particle trajectory calculation was based on the integral of the force balance on a single particle, which was described in a Lagrangian reference frame. This force balance equates the particle inertia with the forces acting on the particle and is given as follows:

$$\frac{d\boldsymbol{u}_{p,i}}{dt} = \boldsymbol{F}_D\left(\boldsymbol{u}_{f,i} - \boldsymbol{u}_{p,i}\right) + \frac{\boldsymbol{g}_i(\rho_p - \rho_f)}{\rho_p} + \boldsymbol{F}_i \tag{3}$$

where i indicates the direction in Cartesian coordinates, $i = \{x, y, z\}$, ρ_p is the particle density, ρ_f denotes the fluid density, $\boldsymbol{u}_{f,i}$ and $\boldsymbol{u}_{p,i}$ indicate the velocity vectors of the fluid phase and particle, respectively, $\boldsymbol{g}_i$ is the gravitational acceleration, and $\boldsymbol{F}_i$ represents the external acceleration acting on the charged particle, which in this model is the electrical force expressed as follows:

$$\boldsymbol{F}_i = \frac{\boldsymbol{E}_i q}{m_p} \tag{4}$$

where m_p indicates the particle mass, and $\boldsymbol{E}_i$ is the strength of the external electric field.

The first term on the right side in (3), $\boldsymbol{F}_D\left(\boldsymbol{u}_{f,i} - \boldsymbol{u}_{p,i}\right)$, is the drag force per unit particle mass due to the relative velocity of the particle and the fluid, where

$$\boldsymbol{F}_D = \frac{18\eta}{\rho_p d^2}\frac{C_D R_e}{24} \tag{5}$$

where, η indicates the viscosity of air, d denotes the particle diameter, C_D is the drag coefficient, and R_e is the relative Reynolds number defined as:

$$R_e \equiv \frac{\rho_f d\left|\boldsymbol{u}_{p,i} - \boldsymbol{u}_{f,i}\right|}{\eta} \tag{6}$$

In addition to the drag force and the electrical force, there is the repulsive force, called space charge force, among nearby charged particles. The calculation of space charge force acting on a particle can be simplified by considering only the nearest neighbors [34]. The space charge force of

two neighboring particles with same charge level of q is given as:

$$F_{spc} \approx \frac{q^2}{4\pi\varepsilon_0 N^{-2/3}} \tag{7}$$

where ε_0 is the permittivity of free space, N is the number of particles per unit volume, determining the distance between the particles. The ratio between the magnitudes of the space charge force and the electrical force can be defined as:

$$\frac{F_{spc}}{F_{X\_square}} = \frac{q}{4\pi\varepsilon_0 E_X N^{-2/3}} \tag{8}$$

In this study, the field magnitude was assumed to be at least 0.15 MV/m and the particle charge level ranges from zero to the Gaussian limit (GL) given by $q_{GL} = \pi\varepsilon_0 E_b d^2$, where E_b is the breakdown field for air. Based on these specifications and providing the particle number concentration is not greater than 10^{12} particles/m^3 [35], the space charge force due to interparticle interactions is several orders of magnitude smaller, for the great majority of particles, compared to the force due to the electric field, and therefore was not included in the simulation.

In addition to the electrical force, the collision of gas molecules with small aerosol particles exerts discrete non-uniform pressures at the particles' surfaces, resulting in random Brownian motion or diffusion [36]. The importance of Brownian motion on particle trajectory via the measurement cell can be judged by calculating the overall distance it travels during its residence inside the measurement cell. The particle root mean square displacement, x_d, in time t due to the Brownian motion in laminar flow is given as ([34]):

$$x_d = \sqrt{2Dt} \tag{9}$$

where D is the Brownian diffusion coefficient for spherical particles and defined as:

$$D = \frac{k_B T_e C_c}{3\pi\eta d} \tag{10}$$

where C_c is the Cunningham slip correction factor, k_B is the Boltzmann's constant, T_e is the environment temperature.

Given a typical velocity at the inlet of 0.02 m/s, a particle residence time inside the measurement cell before reaching the measurement volume is around 1 s. During this time, a particle of 1 μm diameter at room temperature diffuses a distance of about 7 μm, while at the same time travels about 2 cm in the Z direction of the flow [35], which is many orders of magnitude greater. In case of electrical force, the distance, x_p, that a particle will travel in time t due to the electric field is given as,

$$x_p = \frac{E_X q C_c t}{3\pi d\eta} \tag{11}$$

Assuming $E_X = 1.5 \times 10^5$ V/m, $q = 1.6 \times 10^{-18}$C $(10e)$ and the residence time t of 1 s, the displacement of the particle in X direction is around 2 mm, which again is several orders of magnitude greater than the movement due to the Brownian motion. Therefore, in this study, given the particle size range and the experimental conditions, the effect of the Brownian diffusion can be regarded as negligible, which agrees with the literature [35].

The real-time particle velocity in X direction in the square-wave excitation field is given by the following expression (a detailed derivation of the following formulas can be found in [37]):

$$u_{p,x}(t) = \begin{cases} \mu E_X \left(1 - e^{-\frac{t}{\tau}}\right) & 0 \le t < \dfrac{T}{2} \\ \mu E_X \left[2e^{-\frac{t-\frac{T}{2}}{\tau}} - 1\right] & \dfrac{T}{2} \le t < T \\ \mu E_X \left[1 - 2e^{-\frac{t-T}{\tau}}\right] & T \le t < T + \tau \end{cases} \tag{12}$$

where $u_{p,x}(t)$ denotes the real-time particle velocity in X direction and τ is the particle relaxation time defined as

$$\tau = \frac{\rho_p d^2 C_c}{18\eta} \tag{13}$$

μ is the electrical mobility of particle defined as

$$\mu = \frac{qC_c}{3\pi\eta d} \tag{14}$$

Under the influence of the drag and electrical forces in the square-wave excitation field, the particle motion consists of periods of acceleration, deceleration, and the steady state with velocity varying between 0 and its maximum value [38].

III. NUMERICAL METHOD

In this analysis, the 3-D particle trajectories were computed for different simulation conditions using FLUENT software. The calculation of the airflow was accomplished by solving the Navier–Stokes equations. The electric field was implemented using UDFs feature in FLUENT. The trajectories of particles affected by the airflow and the electrical force were calculated using the Lagrangian approach and discrete phase model in FLUENT.

A. NUMERICAL SIMULATION CONDITIONS

The 3-D particle trajectories inside the measurement cell and the number of particles successfully detected inside the measurement volume were computed and analyzed taking into account different particle properties, such as magnitude and polarity of charge and size; air flow conditions, such as the inlet velocity profile; and system configurations including magnitude of the electric field and excitation frequency.

The airflow was assumed to be laminar during the numerical simulations. For each run, the trajectories of a number of particles were calculated assuming that the particle charge, magnitude as well as polarity, size, and initial position were randomly generated with uniform distribution. Each time the particle detection percentage, defined as a ratio of the number of particles successfully detected and validated inside the measurement volume to the total number of particles entering

into the measurement cell, was calculated. The magnitude of the particle charge was computed as follows:

$$q = r_q * q_{GL} \tag{15}$$

where r_q represents the ratio between the charge carried by a single particle and the corresponding Gaussian limit q_{GL} which is proportional to the square of the particle diameter [39]. The particle charges, both polarities, uniformly varied from −GL to GL. Besides, the particle sizes were uniformly distributed random values varying from 0.5 μm to 10 μm. The optical and geometrical system configurations of the PCSA and the other parameters involved in the numerical simulation are presented in Table 1. The environmental

TABLE 1. PCSA simulation parameters.

Parameters	Quantities	Units
Laser wavelength, λ	514.5	nm
Gaussian beam diameter, d_m	1.35	mm
Fringe spacing, i	2.29	µm
Beam intersection angle, θ	12.9	deg
Focal length of front lens, f_L	310	mm
Range of particle charge, q	−GL ~ GL	C
Range of particle size, d	0.5~10	µm
Particle density, ρ_p	0.998×10^3	kg/m^3
Air density, ρ_f	1.225	kg/m^3
Dynamic viscosity of air, η	1.8×10^{-5}	N·s/m^2
Cunningham slip correction factor	≈1	
Size of measurement cell	L_X= 20, L_Y= 20, L_Z= 40	mm
Diameter of inlet	d_{inlet} = 7	mm
Length of electrodes, L_e	20	mm
Width of electrodes, L_Y	20	mm
Electrode-inlet distance, Z_1	10	mm
Size of measurement volume, r_z	97	µm

conditions were assumed to be at room temperature and the atmospheric pressure.

In the simulation, it was assumed that the water–liquid particles travelled in the fluid of air in the measurement cell. The inlet flow velocity profile was assumed to be uniform. The flow velocity was maintained to satisfy a laminar flow condition determined by the Reynolds number value significantly less than 2000. For example, for a given inlet flow velocity of 0.026 m/s and the inlet size of 7 mm the Reynolds number equals to approximately 12. Additionally, the gravitational acceleration in Z direction was taken into consideration.

For each run, for a given simulation condition including the excitation frequency, magnitude of the electric field, and particle velocity at inlet, 5207 bipolarly charged particles were released from the surface of the inlet with random particle properties (charge q and size d), initial positions x_0, y_0, z_0, and initial velocities V_x, V_y, V_z, as listed in Table 2. The flow rate in Table 2 indicates the mass flow rate of the particle stream that follows the trajectory of an individual particle.

As a charged particle with a random charge level, size, initial velocity, and position entered into the measurement cell, the particle motion was mainly influenced by the force due to the electric excitation field and the drag force resulting

TABLE 2. Initial conditions of particle trajectories calculation.

Parameters	Quantities	Units
V_x	0	m/s
V_y	0	m/s
V_z	Particle velocity at inlet, V_{inlet}	m/s
r_q	Uniformly distributed random number from −100% to 100%	%
d	Uniformly distributed random number from 0.5 to 10	µm
x_0	Uniformly distributed random number, $x_0^2 + y_0^2 < \left(\frac{d_{inlet}}{2}\right)^2$	mm
y_0	Uniformly distributed random number, $x_0^2 + y_0^2 < \left(\frac{d_{inlet}}{2}\right)^2$	mm
z_0	−20	mm
Flow rate	10^{-13}	kg/s

from air viscosity. The nature of the measurement system dictated that the majority of the particles terminated on the electrodes or exited via the outlet before being detected inside the measurement volume. Therefore, only a limited number of particles were successfully detected inside the measurement volume. The boundary conditions for the proposed 3-D numerical model are summarized in Table 3. These include

TABLE 3. Boundary conditions for proposed 3-D numerical model.

Surface	Coordinates	Type	Particle
Inlet	z = −20 mm, $x^2 + y^2 < (\frac{d_{inlet}}{2})^2$	Velocity inlet Initial gauge pressure = 0	Escape
Outlet	z = 20 mm, $x^2 + y^2 < (\frac{d_{inlet}}{2})^2$	Outflow	Escape
Electrodes	x = ±10 mm	Stationary walls	Trap
Insulating side walls	y = ±10 mm	Stationary walls	Reflect

the Dirichlet boundary on the inlet velocity and wall boundary used to bound fluid and solid regions.

Domain discretization was implemented using GAMBIT software. The accuracy and smoothness of the solution is determined by the extent of discretization. A sophisticated partition can improve the performance of the simulation. In this model, the whole domain was discretized into 16 000 hexahedral cells, 50 000 quadrilateral faces, and 18 081 nodes.

B. CRITERIA FOR PARTICLE DETECTION AND VALIDATION

After computing the particle trajectories using FLUENT software, the data were analyzed in MATLAB. The particle variables including 3-D positions and velocities, diameters, and IDs of the particle tracks were imported from FLUENT software for further post-processing based on the criteria for particle detection and validation. As previously discussed by the authors in [10], compared to sine-wave, in the square-wave excitation field, the signal processing is less challenging in terms of the requirements of the signal-to-noise ratio and particle residence time within the measurement volume. The signal processing in the sine-wave field is more likely to be affected by the noise and particle position inside the

measurement volume. At least, the particle residence time inside the volume should be greater than one period of the excitation to generate a valid signal burst for the sine-wave excitation. For instance, a short or discontinuous bursts generated by particle moving in and out of the volume in the sine-wave field would not be successfully validated due to the limited burst length.

The particle detection and validation criteria used in this study treat the measurement volume as an ellipsoid [15] instead of a rectangular shape assumed in 2-D simulation [33]. In comparison with the previously published 2-D simulation [33], the 3-D numerical model using combination of MATLAB and FLUENT software is more accurate in terms of the geometry of the measurement cell, the particle transport formulation and detection, and flow velocity calculation.

In the 3-D numerical model, the particle motion inside the measurement cell is validated based on the detection and validation criteria given as follows:

$$\begin{cases} 1)\left[\dfrac{x\,(t)\cos\left(\frac{\theta}{2}\right)}{r_w}\right]^2+\left[\dfrac{y\,(t)\sin\left(\frac{\theta}{2}\right)}{r_w}\right]^2+\left[\dfrac{z\,(t)}{r_w}\right]^2\le 1 \\ 2)x_{max} > -d_x/2+M_{min}i \\ 3)x_{min} < d_x/2-M_{min}i \\ 4)A_{pp} > M_{min}i \end{cases} \tag{16}$$

where $(x\,(t)\,,y\,(t)\,,z(t))$ denote the instantaneous particle position in the Cartesian coordinates, d_x is the diameter of the measurement volume in X direction, $A_{pp}=x_{max}-x_{min}$, x_{min} and x_{max} are the minimum and maximum values of particle position in X direction, respectively. M_{min} indicates the minimum number of fringes which has to be crossed by the particle within the measurement volume. The first inequality in (16) is used to ensure that the particle moves into the domain of the measurement volume. The other inequalities require that a particle travels across the fringes whose number should be no less than M_{min}. Otherwise, it may be difficult to obtain sufficient light scattering in the PDA system. M_{min} was set as 4 in the numerical simulation as recommended in [15].

It is worth noting that when the frequency of the electric excitation is above 200Hz, and the axial velocity of the particle across the measurement volume is less than 0.01 m/s (which is approximately twice the inlet velocity due to change in the flow profile) there is a possibility that more than one period of the particle oscillatory motion could be detected inside the measurement volume of the PCSA resulting in discontinuous burst signals. These discontinuous signals could be misconstrued by the PCSA signal processing unit as independent bursts generated by different particles. The detailed signal processing scheme dealing with such scenarios based on FFT algorithm combined with the evaluation of burst envelope in time domain has been presented by the authors in [38]. Such scenarios, however, can be easily detected in the simulations or all together avoided without resorting to sophisticated signal processing by reducing the excitation frequency or increasing the flow rate and thus present no problem for the PCSA operating within the optimal range of parameters proposed in this paper.

IV. NUMERICAL RESULTS AND DISCUSSION

A. DIFFERENCES BETWEEN INPUT AND DETECTED PROPERTY DISTRIBUTIONS IN THE SIMULATION

In order to conduct an experimental evaluation of the 3-D model, the differences between input and detected particle property distributions in the simulation were compared using the system configuration shown in Table 1. In the experimental procedure, the Medic-Aid Sidestream nebulizer was used to produce the aerosolized dioctyl phthalate droplets [10].

The particle size distribution of the aerosol produced using this method of aerosolization is shown in Table 4. The aerosol inherent charge distribution was measured a few seconds after nebulization. A low flow rate of 0.06 L/min was maintained throughout the measurement to ensure the laminar flow. Experiments were performed in an environment with temperature of approximately 20°C and a relative humidity of approximately 50%. Due to the limitations of the equipment, the higher values of field strength and excitation frequency were not achievable and could not be tested.

TABLE 4. Particle size distribution.

Particle diameter (μm)	Percentage (%)
0.7	9
1.1	11
1.5	26
1.9	21
2.3	8
2.7	12
3.1	9
3.5	4

In the numerical simulation, 100 000 particles in total were injected into the measurement cell from the inlet surface with uniformly distributed initial positions and initial velocities equal to the airflow velocity at the inlet in Z direction. The particle size and charge values of the injected particles followed the same statistical distribution as obtained experimentally [10]. The particle size distribution was split into eight discrete values, as shown in Table 4, while particle charge results were grouped into discrete intervals (bins) shown in Fig. 3. Within each bin, the charge distribution for a given particle size was assumed to be uniform. A comparison between the input and detected property distributions in the simulation, for the naturally charged aerosol, is shown in Fig. 3. The particle count shown in Fig. 3 refers to the percentage of detected particles for a given particle size and charge bin. For example, as shown in Fig. 3 (a), the input property distribution of particle count for the charge values between 0 and 5e is 54%, which means that, in experimental results, 54% of the total number of detected particles of 0.7 μm diameter carried charge from 0 to 5e.

It can be seen from Fig. 3 that the detected property distribution agree well with the input property distribution and show similar trends for different size fractions with the

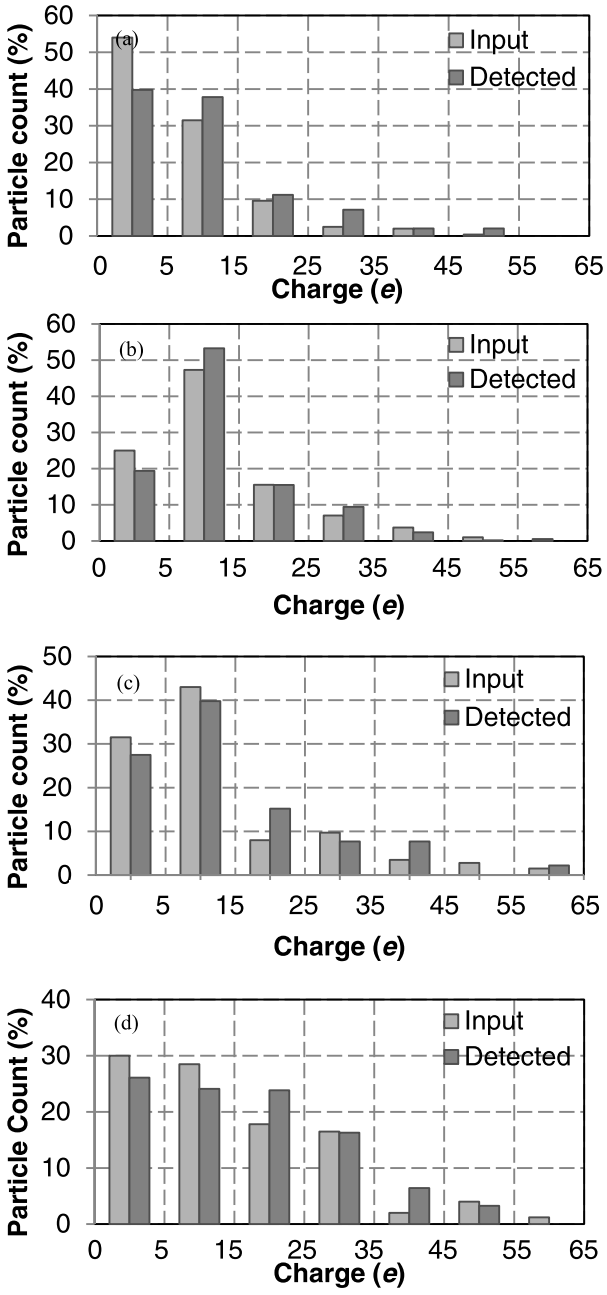

FIGURE 3. Comparison of the particle count for different size fractions between input and detected property distributions in square-wave excitation field: (a) 0.7 μm, (b) 1.1 μm, (c) 1.5 μm, and (d) 1.9 μm.

peak counts occurring at the same charge intervals for both input and detected property distributions. There are also some differences between the input and detected property distributions. These differences can be attributed to random nature of aerosol generation process, the simplifying assumptions and approximations in the numerical model, such as the assumption of uniformly distributed initial particle positions across the inlet. It is important to emphasize that this is not a rigorous validation because the real experimental inlet conditions remain unknown, and any systematic error or biases from the prior experimental measurement are imprinted on the simulation inlet conditions. The difficulty in precise experimental validation of the numerical model is compounded by the fact that the exact nature of the charge and size distribution of the aerosol is not known in advance, and can any be obtained from the measurement, so the numerical simulation has to rely on the experimental data, which itself is subject to a degree of bias and inaccuracy.

B. 3-D NUMERICAL SIMULATION OF CHARGED PARTICLE TRAJECTORIES IN THE MEASUREMENT CELL

This section presents the results of the 3-D numerical investigation. The contours of 3-D airflow velocity field in the measurement cell between the electrodes are shown in Fig. 4(a).

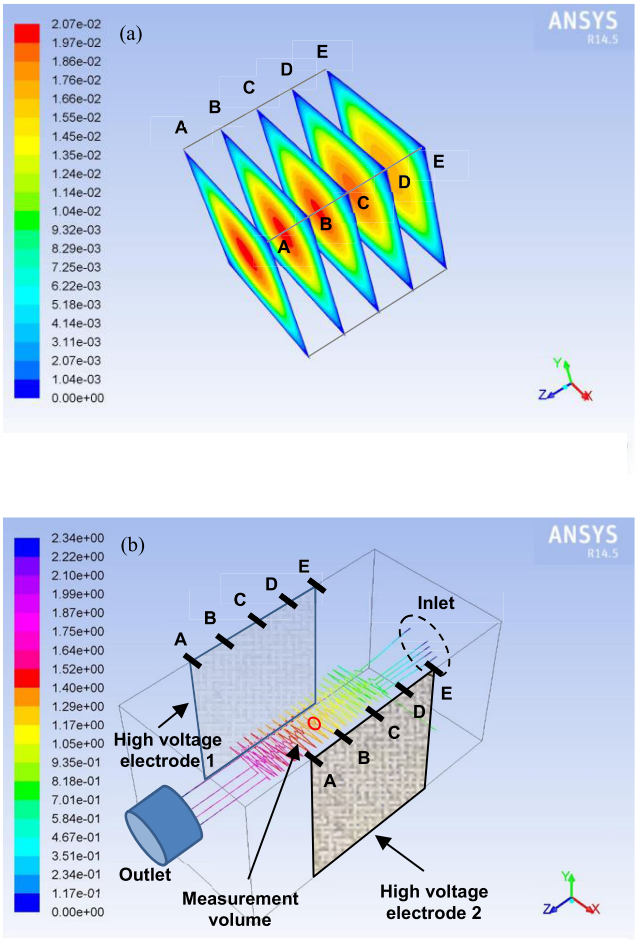

FIGURE 4. (a) Contours of 3-D airflow velocity field, and (b) 3-D trajectories of five particles in the measurement cell in the square-wave field at $V_{inlet} = 0.01$ m/s, $d_{inlet} = 7$ mm, $f = 20$ Hz, and $E = 0.2$ MV/m using FLUENT (Particle traces colored by particle residence time (s)).

As expected, as the flow proceeds through the measurement cell from the inlet to the outlet, the centre line velocity increases along the flow direction with a corresponding decrease in velocity near the walls. It can be seen that the velocity profile of the flow changes from flat to parabolic as it proceeds towards the exit. This flow characteristics increases the residence time of the particles traveling near the wall of the cell and thus the likelihood of these particles to be

deposited on the surface of the electrodes due to the electric field attraction.

One of the advantages of using 3-D numerical model as opposed to 2-D analytical derivation [33] is that it can capture temporal changes in the flow velocity throughout the measurement cell as a function of the inlet and cell geometry as well as the inlet velocity profile, thus enabling more accurate analysis.

To illustrate the influence of particle properties on their relative motion inside the measurement cell, the trajectories of five particles traveling from the inlet to the outlet of the cell are shown in Fig. 4 (b). The color of the particle tracks is indicative of the particle residence time inside the measurement cell, with blue color marking the start of the journey near the inlet and red color the end of the track before exiting via the outlet. The particle charge values used in the simulated tracks are: -4×10^{-16} C, -2×10^{-17} C, 1.8×10^{-15} C, 1×10^{-16} C, and 2×10^{-15} C. The respective particle sizes are 2.3 μm, 0.7 μm, 4.8 μm, 2.8 μm, and 8.8 μm and the corresponding particle initial positions in the X–Y plane are (0, 0), (−3.325, 1.05) mm, (1.325, −0.875) mm, (−0.325, 0.7) mm, and (0.5, −0.525) mm. The simulations were carried out in FLUENT with the excitation frequency of 20 Hz, magnitude of the electric field of 0.2 MV/m, and particle velocity at inlet equals to 0.01 m/s, reaching approximately 0.02m/s velocity near the centre of the cell as the flow becomes fully developed. It can be seen in Fig. 4 that the amplitude of the particle oscillatory motion in X–Z plane varies depending on its electrical mobility, with one particle ending the journey prematurely on the surface of one of the electrodes before it could leave the cell via the outlet.

Following the analysis in FLUENT, the particle trajectories were exported to MATLAB for further processing. The particle trajectories, except for the particle deposited on the surface of the electrode, and the measurement volume in the X–Z plane are shown in Fig. 5 (a). The velocity of the particle with diameter of 8.8 μm and charge of 2×10^{-15} C in X direction is also shown in Fig. 5 (b). The intervals of particle acceleration and deceleration can be seen in the simulated result of particle velocity in one period of the excitation. In the given example, there was only one particle that was successfully detected inside the volume based on the detection and validation criteria discussed in Section III.

To evaluate the effects of the system parameters and particle properties on the transport, detection and validation of charged particles inside the measurement volume, a number of simulations were carried out. In each run 5207 particles were simulated for a given set of conditions. The results of the simulations are discussed in the following sections.

C. PARTICLE DETECTION PERCENTAGE

The influences of different system parameters on the particle detection percentage within the measurement volume were investigated in this section in order to determine the optimal system setup.

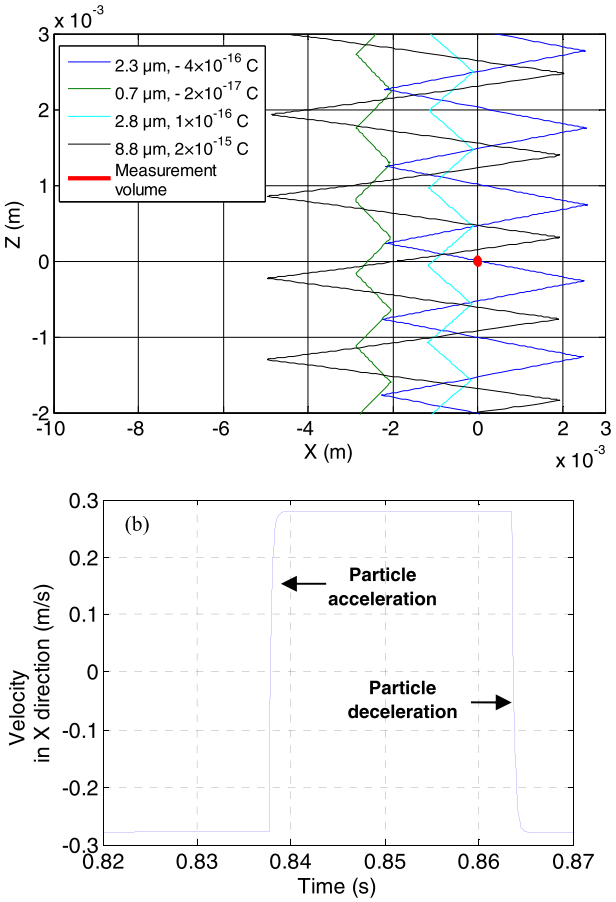

FIGURE 5. (a) Two-dimensional trajectories of particles via the volume in X–Z plane in square-wave field (amplified), and (b) velocity of particle with diameter of 8.8 μm and charge of 2×10^{-15} C in X direction in square-wave field (amplified).

1) THE EFFECT OF EXCITATION FREQUENCY

The results of numerical simulation of the particle detection percentage for different excitation frequencies and particle electrical mobilities are shown in Fig. 6. The absolute values of the electrical mobilities of simulated particles are divided

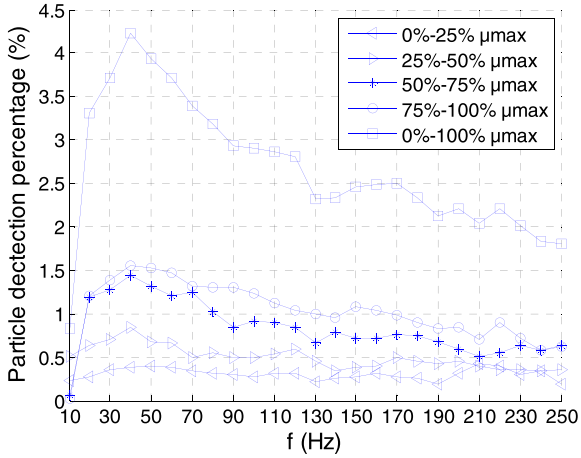

FIGURE 6. The particle detection percentage for different excitation frequencies and particle mobilities (particle velocity at inlet $V_{inlet} = 0.026$ m/s, magnitude of electric field $E = 0.15$ MV/m, and $d_{inlet} = 7$ mm).

into four fractions: 0%-25% μ_{max}, 25%-50% μ_{max}, 50%-75% μ_{max}, and 75%-100% μ_{max}, where μ_{max} denotes the maximum value of particle electrical mobility calculated from (14), corresponding to the Gaussian limit of particle charge. As the excitation frequency becomes higher, the number of detected particles initially increases, achieving its peak value between 30 and 40 Hz, and then gradually decreases as shown in Fig. 6. The particle detection percentage curves exhibit similar trends for different mobility fractions with the peak values of around 0.4%, 0.8%, 1.4%, and 1.6% from the lowest to the highest mobility fraction. The particles carrying greater charge with higher electrical mobilities are statistically more likely to pass through the measurement volume, and therefore be detected by the measurement system, due to their greater amplitude of oscillatory motion. Similarly, as the excitation frequency increases above 40 Hz, the lower amplitude of the particle motion results in lower likelihood of it being detected inside the measurement volume, which leads to a lower particle detection percentage. On the other hand, when the excitation frequency decreases below 40 Hz the particle detection percentage rapidly decreases. This is attributed to the fact that more particles start colliding with the surface of the electrodes before moving into the measurement volume due to considerably larger amplitude of their oscillatory motion.

From Fig. 6, it can be concluded that the optimal range of the excitation frequency in terms of maximizing the particle detection percentage, is from approximately 20 Hz to 70 Hz. The overall particle detection percentage in this range varies from approximately 3.3% to 4.2%. The lower excitation frequencies could be used in case of lowly charged aerosols with mobilities generally not exceeding the 25% μ_{max}, which is often the case for naturally occurring aerosols. It can be also noted that particles with higher electrical mobilities, i.e. more highly charged, are more likely to be detected and measured, which could lead to measurement bias and overestimation of the overall level of charge of aerosol sample and will be discussed the next section of the paper.

2) THE EFFECT OF FIELD MAGNITUDE

The results of numerical simulation showing the particle detection percentage for different field magnitudes and particle electrical mobilities are shown in Fig. 7. With the increase of the magnitude of the electric field the overall number of detected particles, for mobility levels from 0% to 100% μ_{max}, initially increases, achieving its peak value of 4.7% at approximately 0.4 MV/m, and then decreases as the field magnitude becomes higher. A similar trend can be observed, but at different rates, for lower mobility fractions 0%-25% μ_{max} and 25%-50% μ_{max} with the detection reaching peak values of around 1.3% and 1.6% at the field magnitudes of 2.4 MV/m and 0.4 MV/m, respectively. This is to be expected because greater amplitude of the particle motion resulting from increasing field magnitude improves the probability of the particle being detected inside the measurement volume.

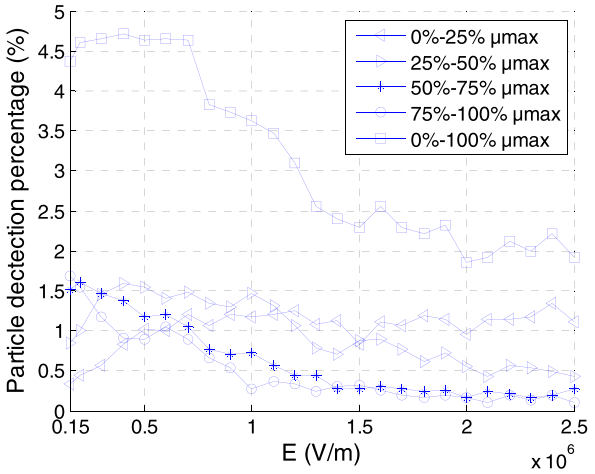

FIGURE 7. The particle detection percentage for different magnitudes of electric field and particle mobilities (particle velocity at inlet $V_{inlet} = 0.026$ m/s, excitation frequency $f = 40$ Hz, and $d_{inlet} = 7$ mm).

On the other hand, for more highly charged particles with higher mobility ranges of 50%-75% μ_{max} and 75%-100% μ_{max}, both particle detection curves show steady decline. This is due to the fact that with the increasing electric field magnitude more highly charged particles are deflected away from the centre of the measurement cell as the amplitude of the particle trajectory in X direction is proportional to the magnitude of the electric field. Consequently, many of these particles are terminating on the electrodes without ever reaching the measurement volume. It can be concluded from Fig. 7 that the optimal range of the magnitude of the electric field in terms of maximizing the particle detection percentage, is between 0.15 MV/m and 1 MV/m with the particle detection percentage varying from around 3.6% to 4.7%.

3) THE EFFECT OF PARTICLE VELOCITY AT INLET

The results of numerical simulation showing the particle detection percentage for different particle velocities at inlet and particle electrical mobilities are presented in Fig. 8.

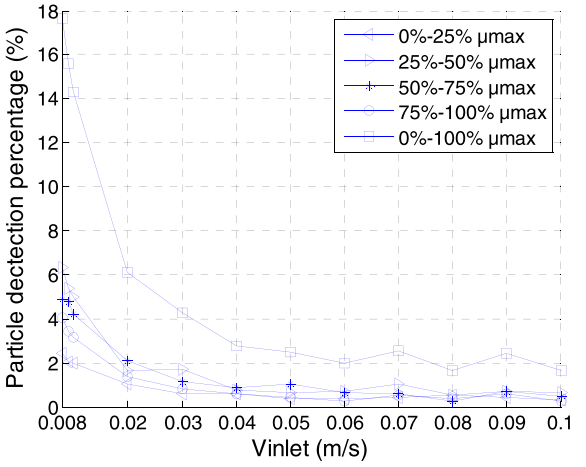

FIGURE 8. The particle detection percentage for different particle velocities at inlet and particle mobilities (excitation frequency $f = 40$ Hz, magnitude of electric field $E = 0.4$ MV/m, and $d_{inlet} = 7$ mm).

The airflow conditions were maintained laminar during the simulation. As shown in Fig. 8, all the curves of particle detection percentage exhibit similar trends for different mobility levels. Initially, the number of detected particles rapidly declines as the particle velocity at the inlet increases. When the inlet velocity exceeds around 0.05 m/s, the number of detected particles levels off. The main reason for this behavior is that the higher inlet velocity results in greater particle displacement in Z direction within one period of the drive excitation and consequently diminishes the probability of particle detection inside the measurement volume.

The simulation results in this section showed clearly that the lower particle inlet velocity the higher number of particles pass through the measurement volume and are successfully validated by the measurement system. However, it is important to bear in mind when setting the appropriate flow rate that very low flow rates lead to longer sampling period and therefore prolong measurement time, which in some cases would prevent capturing dynamic nature of rapidly evolving and dispersing aerosol cloud. The very low flow rate could also increase the likelihood of inter-particle interactions altering the original picture of aerosol charge distribution. On the other hand, very high flow rates could cause turbulence and inaccuracies in the measurement system. Therefore, it seems that a reasonable compromise between these competing requirements would be to aim the flow rate at the value between 0.01 m/s and 0.03 m/s with the particle detection percentage varying from approximately 4.3% to 14.2%.

D. MEASUREMENT BIAS

In previous section of the paper, the analysis and discussion focused on selecting optimal range of system parameters from the point of view of maximizing the overall particle detection percentage. However, the bias of measured particle charge and size distribution is also an important consideration. As demonstrated by the simulation results, the probability of a particle travelling across the measurement volume can be increased by increasing the amplitude of the particle displacement. Since the particle electrical mobility is proportional to the particle charge level, it can sometimes lead to an over representation of highly charged particles in the measurement sample. On the other hand, however, if the amplitude of a particle motion becomes too high, highly charged particles end up colliding with the surface of the electrodes and may never reach the measurement volume, which could lead to under representation of highly charged particles in the aerosol charge distribution measured by the PCSA system. The measurement results, therefore, are likely to be somewhat biased depending on the experimental conditions.

Although, it may not be possible to totally eliminate the measurement bias, it is important to quantify and try to minimize the bias by appropriate selection of the PCSA parameters. A discussion of the effects of system parameters on the particle charge and size measurement bias is presented below. The broad ranges of the excitation frequency (10-250 Hz), electric field strength (0.15-2.5 MV/m) and inlet velocity (0.008-0.1 m/s) shown in Figs. 6-8 have been limited to narrow ranges about the optimal conditions for further investigation in the following sections of the paper.

1) THE EFFECT OF EXCITATION FREQUENCY

In order to evaluate the effect of the excitation frequency on the charge measurement bias, the actual charge distribution of the simulated particles and the charge distribution of detected particles with mobility levels from 0%-100% μ_{max} for different excitation frequencies are compared in Fig. 9. The charge

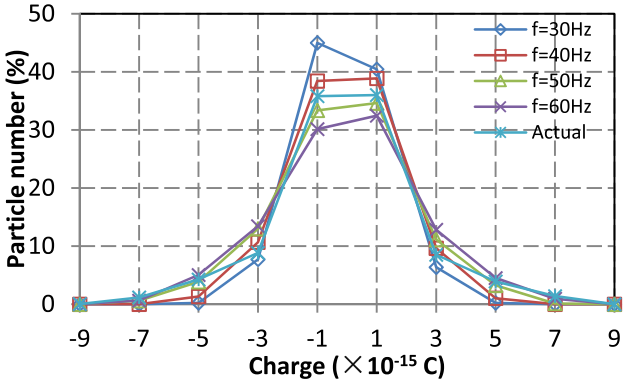

FIGURE 9. Bias of measured charge distribution of detected particles for different excitation frequencies with particle velocity at inlet $V_{inlet} = 0.01$ m/s, magnitude of electric field $E = 0.4$ MV/m, and $d_{inlet} = 7$ mm.

distribution results for different excitation frequencies show that the percentage of highly charged particles detected in the measurement volume for lower frequencies is reduced compared to the detection rate for higher frequencies. Additionally, the percentage of lowly charged particles detected using lower frequency of excitation is slightly increased. The overall charge range of detected particles extends by small margin as the excitation frequency increases. This is to be expected because the increasing excitation frequency reduces the amplitude of particle motion. Subsequently, a highly charged particle is more likely to be captured by the electrodes for lower frequencies due to the greater amplitude of its motion. Thus, the contribution of highly charged particles to the charge distribution is reduced for lower frequencies. For higher frequencies, the decreased amplitude of the particle motion results in a higher probability of detection of highly charged particle inside the measurement volume.

In order to investigate the influence of the excitation frequency on the size distribution measurement bias, the actual size distribution of the simulated aerosol particles and the size distribution of detected particles with combined mobility levels from 0%-100% μ_{max} for different excitation frequencies are shown in Fig. 10. The size range between 0.5 μm and 10 μm has been divided into six bins: 0.5 - 1 μm, 1 - 2 μm, 2 - 4 μm, 4 - 6 μm, 6 - 8 μm, and 8 - 10 μm with the average value for each bin displayed on the horizontal axis. It can be seen that there is a noticeable over representation of medium sized particles in the results of

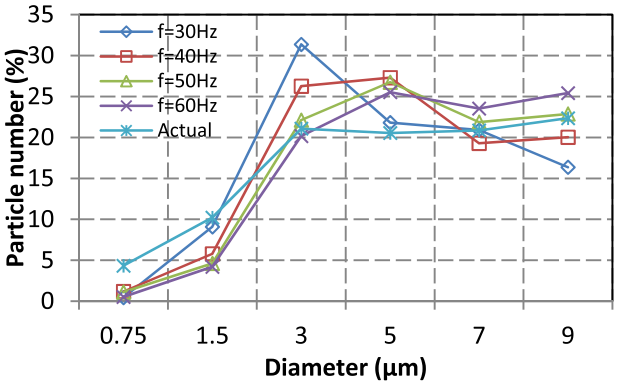

FIGURE 10. Bias of measured size distribution of detected particles for different excitation frequencies with particle velocity at inlet $V_{inlet} = 0.01$ m/s, magnitude of electric field $E = 0.4$ MV/m, and $d_{inlet} = 7$ mm.

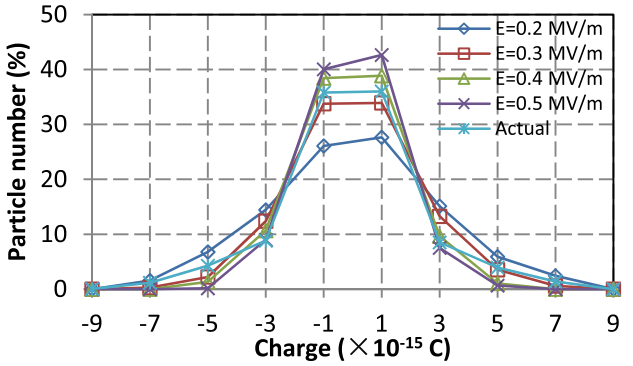

FIGURE 11. Bias of measured charge distribution of detected particles for different magnitudes of electric field with particle velocity at inlet $V_{inlet} = 0.01$ m/s, excitation frequency $f = 40$ Hz, and $d_{inlet} = 7$ mm.

particle size distribution. Since the particle electrical mobility is proportional to the particle charge and size ratio (see (14)) and the Gaussian limit of particle charge is proportional to the square of the particle size [39], the overall electrical mobility range for larger particles is greater compared to smaller particles. Thus, the larger particles are more likely to be trapped by the electrodes due to greater amplitude of their motion. On the lower end of the particle size range the opposite effect dominates the measurement bias. As the electrical mobility of smaller particle decreases, it is more likely for these particles to travel without crossing the measurement volume and being detected. The combination of both of these effects leads to the increased detection rate for the medium sized particles with medium range electrical mobility relative to other particle size fractions. As can be seen in Fig. 10, the particle size measurement bias is also dependent on the selection of the excitation frequency and is getting more pronounced at 30Hz.

Although, due to the nature of the measurement, it is impossible to completely eliminate or accurately predict the measurement bias without knowing a priori characteristics of the measured aerosol, it can be argued that the desirable range of the excitation frequency from the point of view of minimizing the charge and size measurement bias should be between 40 Hz and 50 Hz.

2) THE EFFECT OF FIELD MAGNITUDE

In order to evaluate the effect of the magnitude of the electric field on the charge measurement bias, the actual charge distribution of the entire population of simulated particles with mobility levels from 0% to 100% μ_{max} was compared with the charge distribution of detected particles for different magnitudes of the electric field. The charge distribution curves presented in Fig. 11 show similar trends to those seen in Fig. 9. The charge range of detected particles widens as the field magnitude decreases for similar reasons as already discussed in the previous section. The main reason is that a higher field magnitude results in a greater amplitude of the particle motion, leading to higher likelihood of highly charged particles being captured by the electrodes. On the other hand, lower field magnitudes generate smaller amplitudes of particle motion which means that the lowly charged particles are less likely to be detected inside the measurement volume.

The effect of the field magnitude on the size distribution measurement bias is shown in Fig. 12. The actual size

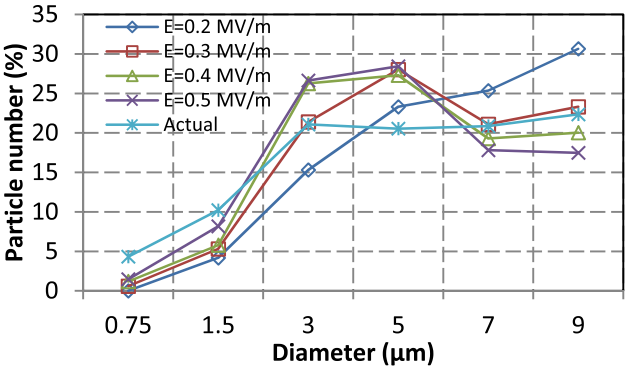

FIGURE 12. Bias of measured size distribution of detected particles for different magnitudes of electric field with particle velocity at inlet $V_{inlet} = 0.01$ m/s, excitation frequency $f = 40$ Hz, and $d_{inlet} = 7$ mm.

distribution of the total number of simulated particles was compared with the size distribution of the detected particles for the entire range of electrical mobility and different field magnitudes. It can be seen that there is an over representation of particles sizes between 2 μm and 6 μm for higher field magnitudes for the similar reasons discussed previously related to the variations in the amplitude of the oscillatory particle motion. The lower field amplitude of 0.2 MV/m curve exhibits a slightly different trend showing under representation of smaller particles and over representation of larger particles detected inside the measurement volume compared with the actual distribution. It is evident in this instance that fewer, smaller, less charged, and therefore less mobile particles are more likely to cross the measurement volume compared to bigger, more charged, and thus more mobile particles. It can be concluded that the optimal range of the field magnitude should be from 0.3 MV/m to 0.4 MV/m from the point of view of minimizing the charge and size measurement bias. However, the field magnitudes outside of this range would also be acceptable for naturally charged aerosols with narrow charged distribution.

3) THE EFFECT OF PARTICLE VELOCITY AT INLET

The actual charge distribution of the simulated particles and the charge distribution of detected particles with mobility levels from 0% to 100% μ_{max} for different inlet velocities are shown in Fig. 13. It was found that the inlet velocity had limited effect on the detected particle charge distribution. However, as demonstrated in Fig. 8, higher flow rate leads to decreasing overall particle detection rate and therefore potentially statistically less significant sample.

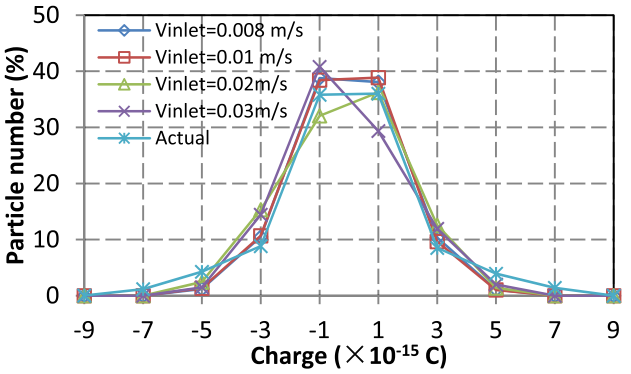

FIGURE 13. Bias of measured charge distribution of detected particles for different particle velocities at inlet with magnitude of electric field $E = 0.4$ MV/m, excitation frequency $f = 40$ Hz, and $d_{inlet} = 7$ mm.

The actual size distribution of simulated particles and the size distribution of detected particles for different inlet velocities are shown in Fig. 14. Generally, similar to previously presented analysis, fewer smaller or larger particles than medium sized particles are detected for different inlet velocities. Although, it can be argued that there is an increase of bias in terms of over representation of larger particles with the increase of inlet velocities, the results seem not sufficiently clear to justify this conclusion.

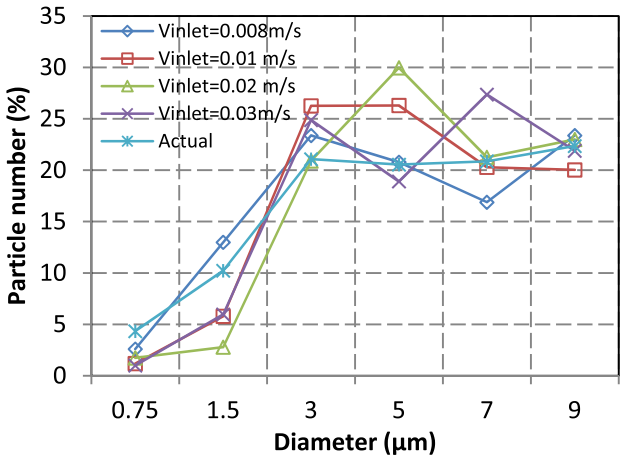

FIGURE 14. Bias of measured size distribution of detected particles for different particle velocities at inlet with magnitude of electric field $E = 0.4$ MV/m, excitation frequency $f = 40$ Hz, and $d_{inlet} = 7$ mm.

V. CONCLUSION

The 3-D numerical modeling of the PCSA measurement system was conducted using FLUENT and MATLAB software to investigate the particle transport and detection inside the measurement volume. The trajectories of a large population of particles were computed in order to evaluate the particle detection percentage inside the measurement volume and the bias in particle charge and diameter distribution in the square-wave excitation field. In order to conduct an experimental evaluation of the 3-D model, the differences between input and detected particle property distributions in the simulation were compared using naturally charged aerosol generated from Medic-Aid Sidestream nebulizer. The detected property distribution agreed well with the input property distribution.

The numerical results demonstrated that particle detection percentage and the bias in particle charge and diameter distribution were affected by different system parameters including the excitation frequency, field magnitude, and particle velocity at the inlet. It was shown that the reduction of the bias of measured charge and size distribution of detected particles can be achieved while maintaining high number of detected particles by an appropriate selection of PCSA parameters, leading to a more representative picture of measured aerosols. The optimal ranges of the excitation frequency, magnitude of electric field, and particle velocity at inlet are between 40 - 50 Hz, 0.3 - 0.4 MV/m, and 0.01 - 0.03 m/s, respectively from the point of view of maximizing the number of detected particles and minimizing the charge and size measurement bias.

Due to the nature of the measurement and the complexity of the interactions between PCSA parameters, particle properties and airflow conditions it is not possible to completely eliminate the bias from particle size and charge distribution measurement. However, considering the results of the simulation, some broad recommendations were provided how to minimize the measurement bias and maximize the particle detection rate. It is important to note that the simulation tests were performed using a very challenging assumption that the magnitude of particle charge was uniformly distributed from 0 to a saturation level for different size fractions. Such a situation is very unlikely to occur in the actual measurements where the majority of particles would likely fall into much more narrow charge distribution, most probably close to the lower end of the charge range spectrum [8], [9]. In such majority of cases, the measurement bias would be considerably smaller than the one presented in this paper due to smaller variation of the amplitude of particle motion. In such cases the square-wave excitation method would be able to provide more representative profile of aerosol size and electrostatic charge distribution.

This 3-D numerical study provided a better understanding of the influence of the effects of different system parameters on the charged particle behavior, detection and validation inside the measurement volume. Future work will focus on extending the developed model by considering non-uniform particle initial velocity and position distributions, as well as different profiles of aerosol charge and size distributions. The signal processing of multi-bursts and discontinuous burst signals will be further investigated to improve the parti-

cle detection and validation performance. Finally, a more generally applicable optimization process to identify an optimal configuration for any PCSA system will be considered. The new approach could include solving multiobjective optimization problem in the presence of conflicting requirements that the design of the measurement system has to satisfy.

REFERENCES

[1] D. Saini, C. U. Yurteri, N. Grable, R. A. Sims, and M. K. Mazumder, "Drug delivery studies on electrostatically charged dry powder inhaler aerosols using a glass bead lung model," in *Proc. IAS Annu. Meeting*, Pittsburgh, PA, USA, Oct. 2002, pp. 2451–2453.

[2] J. Kulon, "Real-time measurement of bipolar charge distribution on pharmaceutical aerosols and powders using phase Doppler anemometry and a bipolar charge measurement system," Ph.D. dissertation, Dept. Syst. Eng., Brunel Univ., Uxbridge, U.K., 2003.

[3] M. Rowland, A. Cavecchi, F. Thielmann, J. Kulon, J. Shur, and R. Price, "Measuring the bipolar charge distributions of fine particle aerosol clouds of commercial PMDI suspensions using a bipolar next generation impactor (bp-NGI)," *Pharmaceutical Res.*, vol. 36, p. 15, Jan. 2019. doi: 10.1007/s11095-018-2544-9.

[4] M. K. Mazumder, R. E. Ware, T. Yokoyama, B. J. Rubin, and D. Kamp, "Measurement of particle size and electrostatic charge distributions on toners using E-SPART analyzer," *IEEE Trans. Ind. Appl.*, vol. 21, no. 4, pp. 611–619, Jul./Aug. 1991.

[5] M. K. Mazumder and K. J. Kirsch, "Single particle aerodynamic relaxation time analyzer," *Rev. Sci. Instrum.*, vol. 48, no. 6, pp. 622–624, 1977.

[6] R. Sharma, D. W. Clark, P. K. Srirama, and M. K. Mazumder, "Tribocharging characteristics of the Mars dust simulant (JSC Mars-1)," *IEEE Trans. Ind. Appl.*, vol. 44, no. 1, pp. 32–39, Jan./Feb. 2008.

[7] L. Zhang and J. Kulon, "Real-time, non-invasive measurement of medical aerosol charge and size distribution: Signal processing strategy, system modelling and optimization," in *Proc. IMTC*, Singapore, May 2009, pp. 457–462.

[8] J. Kulon, B. E. Malyan, and W. Balachandran, "Simultaneous measurement of particle size and electrostatic charge distribution in DC electric field using phase Doppler anemometry," *IEEE Trans. Ind. Appl.*, vol. 39, no. 5, pp. 1522–1528, Sep./Oct. 2003.

[9] R. Beleca, M. Abbod, W. Balachandran, and P. R. Miller, "Investigation of electrostatic properties of pharmaceutical powders using phase Doppler anemometry," *IEEE Trans. Ind. Appl.*, vol. 46, no. 3, pp. 1181–1187, May/Jun. 2010.

[10] L. Zhang and J. Kulon, "Comparative study of square and sine-wave excitation methods for the measurement of aerosol particles charge and size distribution using phase Doppler anemometry," *IEEE Trans. Instrum. Meas.*, vol. 60, no. 4, pp. 1397–1407, Apr. 2011.

[11] C. F. Edwards, K. D. Marx, and W. K. Chin, "Limitations of the ideal phase-Doppler system: Extension to spatially and temporally inhomogeneous particle flows," *Atomization Sprays*, vol. 4, no. 1, pp. 1–40, 1994.

[12] W. Fuchs, H. Albrecht, H. Nobach, C. Tropea, and L. J. W. Graham, "Simulation and experimental verification of statistical bias in laser Doppler anemometry including nonhomogeneous particle density," in *Proc. Int. Symp. Appl. Laser Techn. Fluid Mech.*, Lisbon, Portugal, Jul. 1992, pp. 8.2.1–8.2.6.

[13] R. Rodriguez, F. Murzyn, J. Aubry, A. Mehel, and F. Larrarte, "An innovative LDV data processing method for statistical error corrections. Application to homogeneous and non-homogeneous seeding," *Flow Meas. Instrum.*, vol. 60, pp. 67–77, Apr. 2018.

[14] J. M. Davis and P. J. Disimile, "Optical configuration selection effects on phase Doppler anemometer measurements of glass microspheres," in *Proc. AIAA Aerosp. Sci. Meeting Exhibit*, Reno, NV, USA, Jan. 2005, p. 1410.

[15] H.-E. Albrecht, N. Damaschke, M. Borys, and C. Tropea, *Laser Doppler and Phase Doppler Measurement Techniques*. New York, NY, USA: Springer-Verlag, 2003.

[16] C. M. Sipperley and W. D. Bachalo, "Triple interval phase Doppler interferometry: Improved dense sprays measurements and enhanced phase discrimination," presented at the ILASS-Americas, Pittsburgh, PA, USA, May 2013. [Online]. Available: http://www.ilass.org/2/recent-papers-form.html

[17] Dantec Dynamics A/S, Skovlunde, Denmark. *Laser Doppler Anemometry: Introduction to Principles and Applications*. Accessed: Oct. 5, 2018. [Online]. Available: https://www.dantecdynamics.com/educational-slideshows

[18] W. Lai, J. Shakal, and D. Troolin, "Accuracy, resolution and repeatability of powersight PDPA and LDV systems," TSI Inc., Shoreview, MN, USA, TSI Tech. Note P/N 5001520 (A4), 2013.

[19] J. Davis and P. Disimile, "The effect of lens/aperture selection on phase Doppler anemometer measurements," in *Proc. AIAA Aerosp. Sci. Meeting Exhibit*, Reno, NV, USA, Jan. 2004, p. 604.

[20] J. Desantes, R. Payri, F. Salvador, and V. Soare, "Study of the influence of geometrical and injection parameters on diesel sprays characteristics in isothermal conditions," SAE Tech. Papers 2005-01-0913, 2005, pp. 2511–2518, vol. 5, no. 3.

[21] J. Davis and P. Disimile, "The effect of measurement volume size on PDA measurements of monodisperse glass spheres," in *Proc. AIAA Aerosp. Sci. Meeting Exhibit*, Reno, NV, USA, Jan. 2006, p. 1122.

[22] R. Payri, L. Araneo, J. Shakal, and V. Soare, "Phase Doppler measurements: System set-up optimization for characterization of a diesel nozzle," *J. Mech. Sci. Technol.*, vol. 22, pp. 1620–1632, Aug. 2008.

[23] A. Fischer, T. Pfister, and J. Czarske, "Derivation and comparison of fundamental uncertainty limits for laser-two-focus velocimetry, laser Doppler anemometry and Doppler global velocimetry," *Measurement*, vol. 43, pp. 1556–1574, Dec. 2010.

[24] K. Adamiak, "Numerical models in simulating wire-plate electrostatic precipitators: A review," *J. Electrostatics*, vol. 71, pp. 673–680, Aug. 2013.

[25] Q. Li, Z. Zhang, Z. Wu, Z. Wang, and L. Guo, "Effects of electrostatic field and operating parameters on removing catalytic particles from FCCS," *Powder Technol.*, vol. 342, pp. 817–828, Jan. 2019.

[26] S. Touhami, W. Aksa, K. Medles, A. Tilmatine, and L. Dascalescu, "Numerical simulation of the trajectories of insulating particles in a tribo-aero-electrostatic separator," *IEEE Trans. Ind. Appl.*, vol. 51, no. 5, pp. 4151–4158, Sep./Oct. 2015.

[27] Z. Feng, W. Pan, H. Zhang, X. Cheng, Z. Long, and J. Mo, "Evaluation of the performance of an electrostatic enhanced air filter (EEAF) by a numerical method," *Powder Technol.*, vol. 327, pp. 201–214, Mar. 2018.

[28] H. Osman, G. S. P. Castle, and K. Adamiak, "Numerical study of particle deposition in electrostatic painting near a protrusion or indentation on a planar surface," *J. Electrostatics*, vol. 77, pp. 58–68, Oct. 2015.

[29] N. Farnoosh, K. Adamiak, and G. S. P. Castle, "3-D numerical analysis of EHD turbulent flow and mono-disperse charged particle transport and collection in a wire-plate ESP," *J. Electrostatics*, vol. 68, pp. 513–522, Dec. 2010.

[30] N. Farnoosh, K. Adamiak, and G. S. P. Castle, "3-D numerical simulation of particle concentration effect on a single-wire ESP performance for collecting poly-dispersed particle," *IEEE Trans. Dielectr. Electr. Insul.*, vol. 18, no. 1, pp. 211–220, Feb. 2011.

[31] Q. Lu, Z. Yang, C. Zheng, X. Li, C. Zhao, X. Xu, X. Gao, Z. Luo, M. Ni, and K. Cen, "Numerical simulation on the fine particle charging and transport behaviors in a wire-plate electrostatic precipitator," *Adv. Powder Technol.*, vol. 330, pp. 210–218, Sep. 2018.

[32] M. Dong, F. Zhou, Y. Zhang, Y. Shang, and S. Li, "Numerical study on fine-particle charging and transport behaviour in electrostatic precipitators," *Powder Technol.*, vol. 118, pp. 22–33, May 2018.

[33] J. Kulon, L. Zhang, and M. A. Roula, "Effects of system parameters on particle statistics in aerosol charge and size measurement in oscillatory electric fields," in *Proc. IMTC*, Binjiang, China, May 2011, pp. 1–4.

[34] W. H. Finlay, *The Mechanics of Inhaled Pharmaceutical Aerosols: An Introduction*. San Diego, CA, USA: Academic, 2001.

[35] W. C. Hinds, *Aerosol Technology: Properties, Behavior, and Measurement of Airborne Particles*. New York, NY, USA: Wiley, 1999.

[36] D. Koolpiruck, "Investigation of charged aerosol transport and deposition in human airway model," Ph.D. dissertation, School Eng. Des., Brunel Univ., Uxbridge, U.K., 2005.

[37] L. Zhang, "Design and numerical simulation of the real-time particle charge and size analyser," Ph.D. dissertation, Fac. Adv. Technol., Univ. Glamorgan, Pontypridd, U.K., 2010.

[38] J. Kulon, A. Roula, Z. Al-Daher, and L. Zhang, "An FFT based algorithm for particle charge measurement in the presence of a square-wave excitation field using phase Doppler anemometry," in *Proc. ICIT*, Cape Town, South Africa, Feb. 2013, pp. 1069–1074.

[39] J. A. Cross, *Electrostatics: Principles, Problems and Applications*. Bristol, U.K.: Adam Hilger, 1987.

LU ZHANG was born in Beijing, China. She received the B.Sc. degree in electrical and information engineering from the University of Beijing Technology, Beijing, China, in 2000, the M.Sc. degree in data communications from the University of Sheffield, Sheffield, U.K., in 2006, and the Ph.D. degree from the University of Glamorgan, Pontypridd, U.K., in 2010. Her Ph.D. work addressed the design and numerical simulation of the real-time particle charge and size analyzer.

She is currently a Lecturer with the College of Information Engineering, Shanghai Maritime University, Shanghai, China. Her research interests include medical signal processing, aerosol characterization, and numerical modeling.

JANUSZ KULON (M'06–SM'16) received the M.Eng. degree in electronics and computer science from the Krakow University of Technology, Poland, in 1995, and the Ph.D. degree from the Brunel University of West London, U.K., in 2003. In 2004, he joined the School of Electronics, University of Glamorgan, U.K., as a Senior Lecturer. He is currently an Associate Professor and a Research Group Leader in biomedical engineering and computing with the Faculty of Computing, Engineering and Science, University of South Wales, U.K. He has published over 70 articles in international journals and conference proceedings. His research interests include digital signal processing, biomedical computing, and knowledge-based and expert systems.